IEEE Access
Multidisciplinary | Rapid Review | Open Access Journal

Received June 4, 2020, accepted June 6, 2020, date of publication June 9, 2020, date of current version June 18, 2020.

Digital Object Identifier 10.1109/ACCESS.2020.3001039

Microwave Imaging for Breast Cancer Detection: The Discrimination of Breast Lesion Morphology

HAOYU ZHANG
School of Naval Architecture and Mechanical-Electrical Engineering, Zhejiang Ocean University, Zhoushan 316022, China
e-mail: haoyu19871202@163.com

This work was supported in part by the Zhejiang Provincial Natural Science Foundation of China under Grant LQ18E070004, in part by the Zhejiang Ocean University Scientific Research Start-up Funding under Grant 21045012815, and in part by the Research on The Policy of Marine Electronic Information Industry under Grant 21048005216.

ABSTRACT Radar based microwave imaging system is proposed and used for breast cancer detection. Tumour location can be detected based on high dielectric differences between tumour and surrounding tissues. In clinical medicine, malignant tumour usually has more irregular morphology than benign tumour. However, previous work has ignored the discrimination between benign and malignant tumours, and this issue is solved in our work. In this paper, two major novel contributions are presented. Firstly, a complex natural responses (CNRs) method is proposed for discrimination between the benign and malignant tumours. The CNRs of the tumour show a unique feature that the CNRs only depend on the morphological appearance of the tumour. Simulation results show that the use of the CNRs can successfully discriminate between a 5 mm radius spherical benign tumour and a 5 mm average radius malignant tumour with a spiculated periphery. Secondly, microwave images of the benign and malignant tumours are created by a proposed mono-static imaging system which uses a single Vivaldi antenna to scan the breast. Both benign and malignant tumour positions can be correctly indicated from the images.

INDEX TERMS Breast cancer detection, microwave imaging, complex natural responses (CNRs).

I. INTRODUCTION

Breast cancer is a serious health issue for women [1]–[12]; however, with early cancer detection there are great chances of survival. X-RAY mammography [2] is the most common technology used in breast cancer detection, creating images of cancerous breast using ionizing radiation, with cancerous tissues located for further treatment. However, the limitations of X-RAY mammography [3], such as a number of false-negative results have resulted in research into microwave imaging based breast cancer detection. Microwave imaging based breast cancer detection relies on high differences in electromagnetic properties between healthy and cancerous tissues [1]–[9]. Radar based imaging originates from ground-penetrating radar (GPR) and was proposed for breast cancer detection in 1996 by Benjamin [6]. This radar based microwave imaging aims to determine the presence of tumour by creating images of back-scattering signals, distinguishing tumours from surrounding healthy tissues due to the high dielectric differences. Compared with the X-RAY mammography, the use of the microwave imaging system can greatly reduce the risk of exposure to strong radiation since the radiation intensity of the microwave imaging system is similar to that of the RF devices such as mobile phone, WIFI or radio, which means the microwave imaging is safe for human. Radar based imaging system includes two prototypes, known as multi-static radar and mono-static radar systems, respectively. Most multi-static radar imaging systems [7]–[9] configure an antenna array to surround the breast, with electromagnetic pulses transmitted and received alternately by each antenna. Mono-static radar imaging system [11] uses a single antenna or an antenna pair to scan the breast with mechanical movement. Received signals are used to create microwave images with tumour highlighted.

Previous publications [1], [3], [5], [6], [8]–[11] assume tumour phantom with uniform shape, such as sphere or ellipsoid. This assumption simplifies the research process, but ignores the different morphological appearance of benign and malignant tumours. In clinical medicine, malignant tumour usually has an irregular surface and spiculated periphery, while benign tumour has smoother surface and roughly spherical morphology [12]. It has been shown in the literature [13], [14] that buried objects such as landmines can be identified by analyzing their complex natural responses (CNRs), which are extracted from the backscatter signals when the object is illuminated by a short electromagnetic pulse.

The associate editor coordinating the review of this manuscript and approving it for publication was Andrei Muller.

This work is licensed under a Creative Commons Attribution 4.0 License. For more information, see https://creativecommons.org/licenses/by/4.0/

The CNRs of objects have distinctive characteristics [13]–[16] such as being independent of the antenna position, the polarization of the incident wave and only being determined by the properties of object such as shape and materials leading to differences in dielectric constant and conductivity. Similarly, a breast tumour can be considered as an object buried in a lossy medium. Benign and malignant tumours can then be distinguished by investigating their CNRs.

In preliminary studies of the discrimination of breast lesions, the morphological features of lesions have been classified [15], and tumours with different conductivity and size have been considered [16]. However, in [16], the tumour is still assumed to have a uniform ellipsoid shape, and the morphology of the benign and malignant tumour is not considered. In [15], [16], the work is only carried out based on a 2-D scenario. Besides, the incident electromagnetic wave is assumed to be a plane wave. However, radar based breast cancer detection is based on the near-field scenario, where the shape of the incident wave varies with radiation distance and the plane wave can only be assumed in the far-field. Furthermore, transmitting and receiving antennas are not considered, but are replaced by an incident wave and an observed point. Actually in the near-field, the impendence of antenna is strongly affected by adjacent objects such as breast, which cannot be replaced by an incident wave and an observed point in practice. In addition, microwave images of malignant and benign tumours have not been studied. In general, [15], [16] have used an idealized model, but a more realistic model based on a 3-D, near-field, antenna system scenario is still required. To the best of our knowledge, these limitations have not yet been addressed.

This paper proposes a method using complex natural responses (CNRs) to discriminate between the benign and malignant tumours based on a mono-static prototype radar system with 3-D simulation. Initially, two breast phantoms, one with a benign tumour and another with a malignant tumour, are proposed. Secondly, the mono-static radar system is proposed, with its performance described in terms of scatter parameters. These two breast phantoms are then measured by the imaging system, with backscatter signals recorded in the time and frequency domains. Three-dimensional images of the breast phantoms are created using the backscatter signals to indicate tumour position. Finally, the CNRs of benign and malignant tumours are analyzed to characterize their morphological appearance. The major novel contribution in this paper is to discriminate between benign and malignant tumours based on their morphology in a realistic 3-D scenario by using the proposed CNRs method. Results indicate that the use of the CNRs can successfully discriminate between a spherical benign tumour with a radius of 5 mm and a speculated periphery with an average radius of 5 mm. Further novel contributions presented in this paper include: 1) comparison of microwave images of the malignant and benign tumours; 2) comparison of the tumour responses based on different working frequencies; 3) identification of the influence of the breast phantom on the antenna; 4) comparison of resulting image resolutions based on the time and frequency domains and 5) proposing a new skin reflection and clutter removal method.

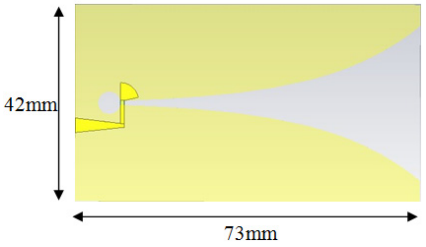

FIGURE 1. The geometry of the Vivaldi antenna.

II. THE BREAST PHANTOM AND EXPERIMENT SETUP

A. THE BREAST PHANTOM DESIGN

The phantom design can be simplified in an approximation as a multi-layer model, with each layer corresponding to a particular bio-layer [17], [18]. For example, the human head can be modeled as a combination of skin, fat, bone, grey matter and white matter layers. The breast can also be modeled as a combination of skin and fat layers. Tumours and glands can then be inserted into the fat layer. Several parameters indicate the properties of layers, with the most important being each layer's dielectric constant $\varepsilon_r(\omega)$, which is frequency dependent. The dielectric constant $\varepsilon_r(\omega)$ of a bio-layer can be derived by the Cole-Cole model, given by (1) [17], which shows that the dielectric constant is reduced as working frequency increases:

$$\varepsilon_r(\omega) = \varepsilon_\infty + \frac{\varepsilon_s - \varepsilon_\infty}{1 + (i\omega\tau)^{1-\alpha}} \tag{1}$$

where, $\varepsilon_r(\omega)$ is the complex dielectric constant, ε_s and ε_∞ are the static and infinite frequency dielectric constants, ω and α are the angular frequency and exponent parameter, τ is the time constant.

B. EXPERIMENTAL SETUP

The Finite Difference Time Domain (FDTD) method is used to simulate breast cancer detection. A Vivaldi antenna is designed first. The dimensions of the Vivaldi antenna are 73mm × 42mm, with the geometry shown in Fig. 1. Copper ground plate and feeding microstrip line are on both sides of the substrate. The performance of the Vivaldi antenna in terms of reflection coefficients is shown below. Two pathological breast phantoms (Fig. 2) are then created. The hemispherical breast phantoms consist of a 2 mm skin layer and a 68 mm fat layer, with a benign tumour and a malignant tumour embedded in the fat layer.

The simulations are concluded by first placing the Vivaldi antenna close to the breast phantom, then rotating it on the central axis (using the notations X, Y, Z and O_{xyz} in Fig. 2 (a)) along the surface of the breast phantom. Fig. 2 (b) indicates the rotation tracks of the Vivaldi antenna. Each point corresponds to a Vivaldi antenna stop location. The front centre of the Vivaldi antenna stops at these points, with the scattering

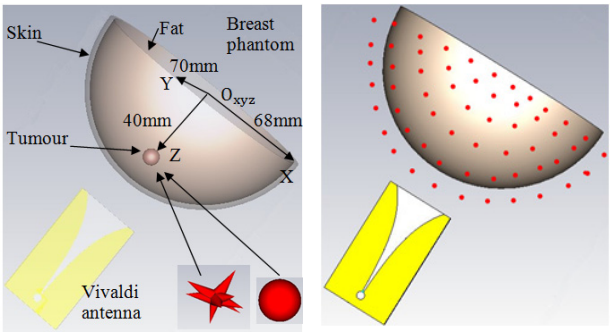

FIGURE 2. (a) The prototype of the imaging system and (b) the Vivaldi antenna movement position.

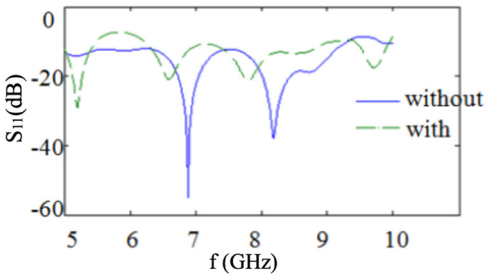

FIGURE 3. The simulated S_{11} with and without the breast phantom presence.

parameters recorded, and then it moves to the next stop point. This procedure is repeated 98 times, giving 98 sets of scattering parameters recorded in both the frequency and time domains which are then used to create microwave images of the breast phantom with the tumour highlighted.

Fig. 3 shows the simulated scatter parameters of the Vivaldi antenna with and without the presence of breast phantom, based on the Finite Difference Time Domain (FDTD) method. The −10 dB working region extends from 5 to 10 GHz when no phantom is used. It is also observed that with the breast phantom present, the scatter parameter still ranges from 5 to 10 GHz although there are some discrepancies around 6 GHz. This means that the breast phantom has very little effect on the impendence of the Vivaldi antenna in the near-field.

III. SIGNAL PROCESSING

A. ELECTROMAGNETIC SCATTERING

When an incident wave with electric field $\overrightarrow{E^i}$ is incident on an object in free space, the representation of the scattered wave, $\overrightarrow{E^s}$, in the frequency domain can be expressed as [19], [20]:

$$\overrightarrow{E^s}(\bar{r}, s) = \int_{v'} \overline{\overline{G}}(\bar{r}, \bar{r}', s) \cdot \vec{J}(\bar{r}', s) \mathrm{d}v' \tag{2}$$

where $\vec{J}$ is the induced current of the object, $\overline{\overline{G}}$ is the dyadic Green function, and $\bar{r}, \bar{r}'$ represents the observation point of the scattered field and the points inside the volume of the object. This equation is in the frequency domain, with $s = jw$. The time-domain expression of (2) [21] is:

$$\overrightarrow{E^s}(\bar{r}, t) = \int_{v'} \overline{\overline{G}}(\bar{r}, \bar{r}', t - R/v) \otimes \vec{J}(\bar{r}', t) \mathrm{d}v' \tag{3}$$

where v is the propagation speed in the medium, and $R = \left|\bar{r} - \bar{r}'\right|$ represents the distance between the point in the object and the observation point.

Electromagnetic scattering can be specified by the Rayleigh, resonance and optical regions using the ratio of relative scatter object dimension to the wavelength of incident wave [22]. Equation (4) shows the relation between the scattering region, the scatter object dimension and the wavelength of the incident wave:

$$\text{Scattering region} = \begin{cases} \dfrac{D}{\lambda} \ll 1 & \text{Rayleigh region} \\ 0.5 < \dfrac{D}{\lambda} < 10 & \text{Resonance region} \\ \dfrac{D}{\lambda} > 10 & \text{Optical region} \end{cases} \tag{4}$$

where D is the scatter object dimension, and λ is the incident wavelength.

For the breast cancer detection based electromagnetic propagation mechanism, the propagation speed and incident wavelength depends on the dielectric constant of the propagation medium, which can be expressed as (5):

$$\lambda = \frac{2\pi \cdot v_m}{\omega} = \frac{2\pi \cdot c_0}{\omega \cdot Re\left[\sqrt{\varepsilon_r(\omega)}\right]} \tag{5}$$

where v_m is the wave propagation speed in the medium, ω is the angular frequency, $\varepsilon_r(\omega)$ is the complex dielectric constant of the medium expressed in (1) and c_0 is the wave propagation speed in vacuum. Table 1 shows the calculated wavelength in the vacuum and different breast layers (skin, fat, tumour) when the frequency of the incident wave ranges from 5 to 10 GHz as well as the ratio of the scatter object dimension D to the wavelength of the incident wave λ, D/λ. It should be noted that, in the case of breast cancer detection, λ is the incident wave for each layer. For example, D/λ for the skin layer, and λ is the wavelength in free space, rather than the wavelength in the skin layer due to the incident wave being in free space. Likewise, D/λ for the fat and tumour layers, λ are the wavelength in the skin and fat layers, respectively. Table 1 also indicates that the skin layer scattering mechanism involves both the resonance and optical regions, while the fat layer scattering involves the optical region, and the tumour scattering involves the resonance region.

In the optical region, the specular reflection from surface of the illuminated object contributes most of the scattered wave. The scattering mechanism in the optical region can be solved using the theories of Geometrical Optics (GO) or Physical Optics (PO) [22]. The resonance scattering mechanism in the resonance region is of interest in this paper, since the tumour scattering involves this region. Fig. 4 shows the basic electromagnetic scattering mechanism. An incident electromagnetic wave illuminates a perfect conducting sphere (PCS) causing a specular reflection first, and followed by a travelling wave

TABLE 1. The minimum and maximum wavelength in different layers of breast.

	Vacuum	Skin	Fat	Tumour
Min (λ) mm	30	10	26	8
Max (λ) mm	60	11	28	9
D	N/A	440	427	31
Min(D/λ)	N/A	7	39	1.1
Max(D/λ)	N/A	15	43	1.2

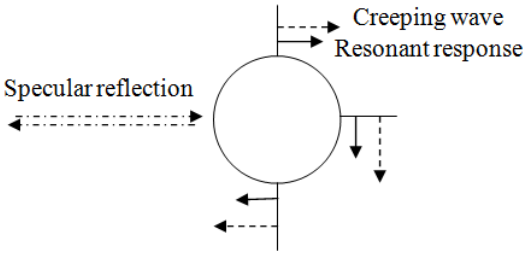

FIGURE 4. The electromagnetic scattering mechanism.

propagating around the PCS. This travelling wave propagates around the sphere until reaching the specular point, with a backscattered wave generated, and this combines with the specular reflection constructively or destructively, to create a creeping wave. This process is also called early time response (ETR). The second stage comes with the induced current in the sphere. This induced current is excited by the generated induced electric field which resists the incident wave. This induced electric field is also called the resonant response, or late time response (LTR).

Baum [19], [20] proposed a mathematical representation based on the singularity expansion method (SEM) to describe the induced current generated by the incident wave in terms of the expansion of Laplace domain singularities. The induced current based on the SEM is expressed as (6):

$$\vec{J}(\bar{r}', s) = \sum_{n=1} \frac{E^i(s_n)\eta_n(\hat{k}^i, \hat{e}^i)v_n(\bar{r}')}{s - s_n} e^{-(s-s_n)t_L} + \bar{F}(\hat{k}^i, \hat{e}^i, s) \tag{6}$$

where $\vec{J}$ and E^i are the induced current and incident electric field respectively, t_L is the late time Turn On time, $s_n = \sigma_n + j\omega_n$ is the resonant response in the pole representation, σ_n and ω_n are the damping constants and resonant frequencies, η_n is the coupling coefficient, $\hat{k}^i$ and $\hat{e}^i$ are the direction and polarization of the incident wave. v_n is the natural mode of the resonant response, $\bar{F}$ is the ETR. Substituting (6) into (3) as:

$$\vec{E^s}(\bar{r}', s) = \sum_{n=1} \frac{\overline{R'_n}(\hat{k}^i, \hat{e}^i, \bar{r})}{s - s_n} e^{-(s-s_n)t_L} + \overline{W}(\hat{k}^i, \hat{e}^i, \bar{r}, s) \tag{7}$$

where $\overline{R'_n}$ is the residue of the pole, $\overline{W}$ is the ETR. The time domain of (8) is

$$\vec{E^s}(\bar{r}, t) = \sum_{n=1} \overline{R'_n}\left(\hat{k}^i, \hat{e}^i, \bar{r}\right) e^{s_n t} u(t - t_L) + \overline{W_e}(\hat{k}^i, \hat{e}^i, \bar{r}, t) \tag{8}$$

where t_L is the resonant response or LTR Turn On time, which means the boundary between the ETR and LTR. For (7) and (8), the first and second terms are the LTR and ETR, respectively. The ETR term is an entire function, and the LTR is represented by the expansion of poles. Here the poles $s_n = \sigma_n + j\omega_n$ are independent of the direction and polarization of the incident wave and only determined by the properties of the object in terms of shape, materials, etc [23]. This distinctive feature of s_n can be used to describe the object of interest in terms of the LTR in transient scatter signals. Several methods [24]–[27] have been proposed for the extraction of the poles, such as Prony's method, Covariance method and Matrix Pencil Method (MPM). In this paper, the MPM is used to extract the poles of the transient scatter signal, due to its robust pole estimation in noisy environment.

B. THE TRANSIENT SIGNAL

The electromagnetic scattering mechanism has been analyzed by considering the tumour resonance response in a lossy medium (breast tissue). The skin and fat scattering mechanism mainly involves the optical region, which contributes the ETR in the received time domain signals. However, the tumour scattering mechanism only involves in the resonance region, which contributes the LTR. Besides, the tumour response in the resonance region only depends on its properties, such as morphology and dielectric constant. This unique feature can be used to distinguish between benign and malignant tumours.

Fig. 5 (a) shows the received transient scattering signals. These signals are obtained using the proposed mono-static radar imaging system, and each corresponds to as top points (the points in Fig. 2) of the Vivaldi antenna. These signals are too close to be distinguished. Hence, a transient scattering signal when the Vivaldi antenna stops at the centre of the breast phantom (X = 0, Y = 0, Z = 80) is selected, as shown in Fig. 6 (b).

The first step is to determine the boundary between the ETR and the LTR, which is also the turn on time t_L. In [27], the turn on time t_L is defined by assuming that the transient response of a scattering object is observed in free space (9):

$$\begin{aligned} t_A &= R/c \\ t_B &= t_A + L_t/c \\ t_{Lmax} &= L_{max}/c \\ t_L &\geq 2t_A + 2t_{Lmax} \geq 2t_B + t_{pw} \end{aligned} \tag{9}$$

where t_A and t_B indicate the time when the wave front reaches the points A and B, L_{max} is the maximum dimension of the scattering object, t_{pw} is the width of the incident pulse, and t_L is the turn on time. In this paper, Equation (9) is used to estimate the t_L in the cancerous breast phantom by applying the following necessary

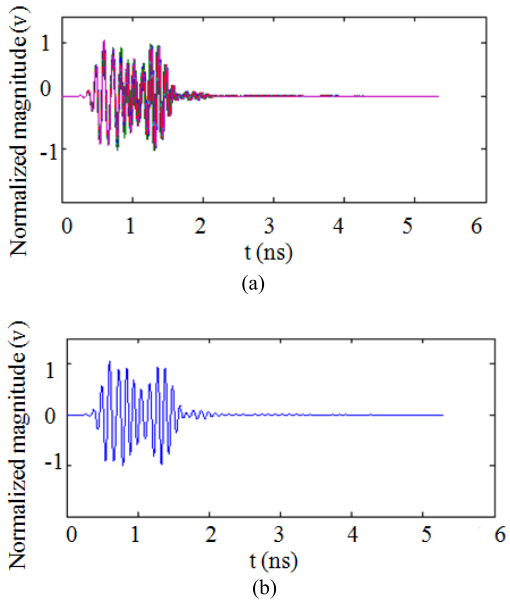

FIGURE 5. (a) The received transient scattering signals and (b) selected signal.

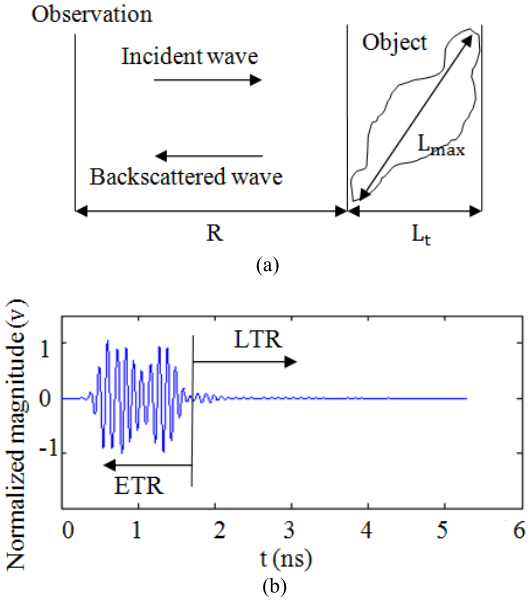

FIGURE 6. (a) The free space scattering configuration (b) The transient scatter signal of the cancerous breast phantom.

modifications (10):

$$\begin{aligned} t_A &= R_v/c + R_s/v_s + R_f/v_f \\ t_B &= t_A + L_t/c \\ t_{Lmax} &= L_{max}/v_f \\ t_L &\geq 2t_A + 2t_{Lmax} \geq 2t_B + t_{pw} \end{aligned} \tag{10}$$

where R_f, R_s, R_f indicate the travelling path of the wave in free space, skin and fat layers. v_s and v_f are the wave velocities in the skin and fat layer, respectively. $L_{max} = L_t$ indicates the diameter of the tumour. t_{pw} is the width of the incident pulse. Fig. 6 (b) shows the turn on time t_L as well as the ETR and the LTR. The ETR contains the specular reflections and forced response generated by the induced current. The LTR only contains the induced current at the natural resonance frequency. Hence, the LTR can be decomposed to the sum of the damping sin functions, with their frequencies corresponding to the natural response of the object. The damping factors can then be used to distinguish between benign and malignant tumours.

However, the determination of the boundary between the ETR and LTR is based on prior knowledge of the object (tumour) position. Hence, for the microwave image based cancer detection, a solution can be to first create the cross-images of the breast phantom to indicate the tumour position, and then to use the tumour position to estimate the boundary. A time window is then designed to remove the ETR and unwanted clutter. The remaining LTR part will be used to extract the natural response of the tumour.

C. THE CREATION OF THE BREAST CROSS-SECTION IMAGES

A set of received transient signals is shown in Fig. 7 (a). The tumour response is too weak compared with the skin reflections, and can easily be drowned out in the clutter. The first step of the creation of the breast cross-section images is to subtract the skin effect and clutter. To solve this problem, most studies suggest measuring the transient response signal of a breast phantom without the presences of tumour. This calibration signal contains only the skin response and other unwanted clutter. The tumour response can then be extracted by subtracting the calibration signal. This process can be expressed by $S_{tumour} = S_{rece} - S_{cal}$, where S_{rece} and S_{cal} indicate the received transient signal and the calibration signal respectively. However, this method cannot be applied in clinical practice since the identical breast without a tumour is not unavailable. Here, we present a new method to eliminate the skin effect and clutters.

The mono-static radar based cancer detection rotates the antenna to scan the breast phantom, and the received transient signal can be expressed by: $S^i_{rece} = S^i_{skin} + S^i_{tumour} + S^i_{clutter}$ where S^i_{rece}, S^i_{skin}, S^i_{tumour} and $S^i_{clutter}$ indicate the received signal, skin effect, tumour response and clutters, respectively. The notation i indicates one of the antenna stop positions. We define the calibrated signal as:

$$\begin{aligned} S^i_{cal} = (S^i_{rece} - S^{i+1}_{rece} + S^i_{rece} - S^{i-1}_{rece} \\ + S^i_{rece} - S^{i+2}_{rece} + S^i_{rece} - S^{i-2}_{rece})/4 \end{aligned} \tag{11}$$

where S^{i+1}_{rece}, S^{i-1}_{rece}, S^{i+2}_{rece} and S^{i-2}_{rece} indicate the adjacent antenna positions. Since the antenna rotates in fixed small steps while maintaining a constant distance to the skin layer, the skin effect and clutters are also constant. Hence, taking the average value of the subtraction of the four adjacent signals eliminates the unwanted response while enhancing the tumour response. This method can be used with both the time and frequency domain signals.

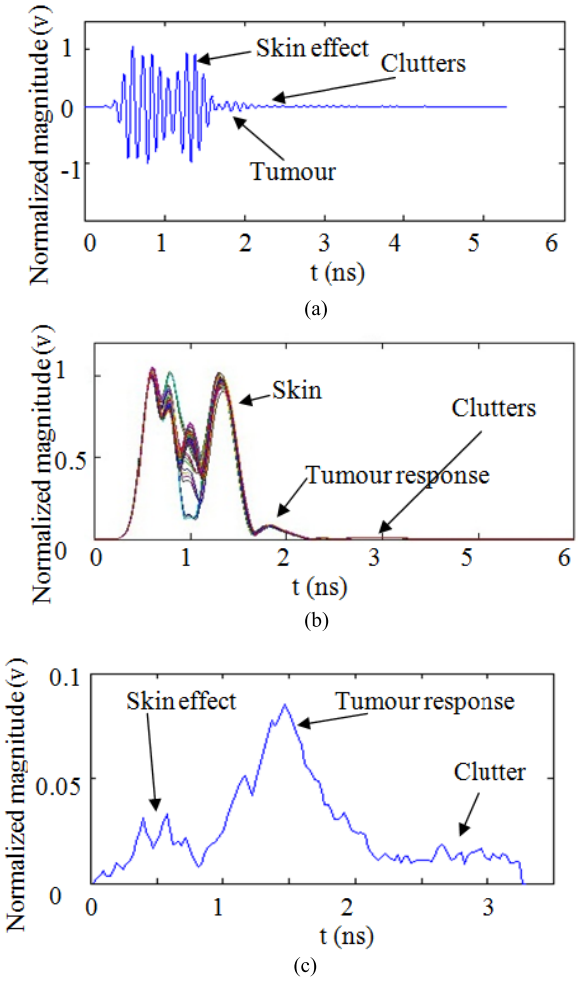

FIGURE 7. (a) The received transient scattering signals and (b) the envelope of the analytical signals and (b) tumour response after calibration.

1) For the image creation based on the transient signals, instead of directly using the received signal S(t), we employ its analytical signal S^{+}(t), represented as:

$$S^{+}(t) = S(t) + j\mathrm{H}\{S(t)\} \tag{12}$$

where, $S(t)$ is the original received signal as the real part, and H$\{S(t)\}$ is the imaginary part which is obtained from the Hilbert Transform of $S(t)$:

$$\mathrm{H}\{S(t)\} = \frac{1}{\pi}\int_{-\infty}^{+\infty}\frac{S(\tau)}{S(t-\tau)}\mathrm{d}(\tau) \tag{13}$$

Fig. 7 (b) shows the envelope of the analytical signal. This is used for the further processing. The use of the analytical signal provides a more average representation of the received signal, which more clearly indicates the skin, tumour and clutter compared with the original received signal. As seen from Fig. 7 (b), the skin effect is very strong compared with the tumour response, so we need to calibrate the received signals by removing the skin effect. In our system, the antenna rotates around the breast to transmit and receive the signals while maintaining a constant distance to the skin layer. So,

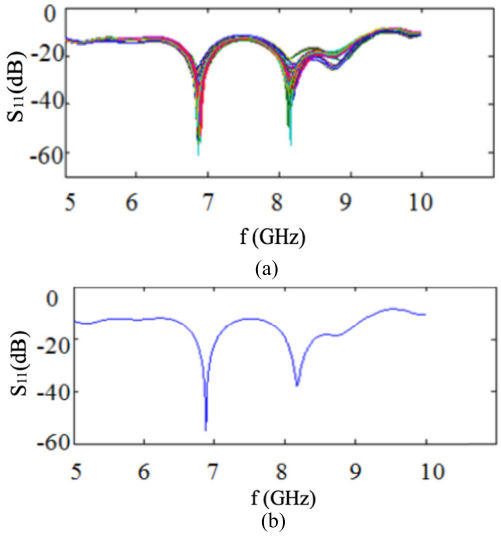

FIGURE 8. The received S_{11} parameters at (a) each of the stop point and (b) the center of the breast phantom (X = 0, Y = 0, Z = 80).

the amplitude of the skin effect part of all the received signals are very close. However, the amplitude of the tumour response part becomes stronger when the antenna rotates close to the tumour and when the antenna rotates away from the tumour, the amplitude becomes weak. According to this phenomenon, firstly, we calculate the average amplitude of the skin effect part (also called the ETR part as seen in Fig. 6 (b)) using all received signals and consider the averaged amplitude as a calibration signal. Then, each received signal is calibrated by subtracting this calibration signal. As seen from Fig. 7(c), the skin effect and unwanted clutter are significantly eliminated. The peak of the tumour response is used to create the breast phantom images in the next section.

2) Fig. 8 (a) shows the received S_{11} parameters. Each corresponds to a stop point when the Vivaldi antenna is moving to scan the breast phantom. Fig. 8 (b) shows the S_{11} when the Vivaldi antenna stops at the centre of the breast phantom (X = 0, Y = 0, Z = 80). The skin effect and clutter can be eliminated by using (11) and the resulting values of the calibrated S_{11} at 5, 7, 9 GHz are used to create the cross images of the breast phantom in the next section.

IV. THE RESULTS

This section presents the 3-D cross-images of the cancerous breast phantoms. The received transient signals and the S_{11} parameters have been collected at different stop points when the Vivaldi moves to scan the breast phantom. Both transient signals and frequency domain signals show stronger amplitude when the Vivaldi antenna moves close to the tumour, due to the high dielectric differences between it and the surrounding tissues. Each of the stop points corresponds to a received signal in both time and frequency domains (transient signals and S_{11}, as shown in Fig 7 (b) and Fig 8 (a)). Hence, the cross-section images of the breast phantom can be created

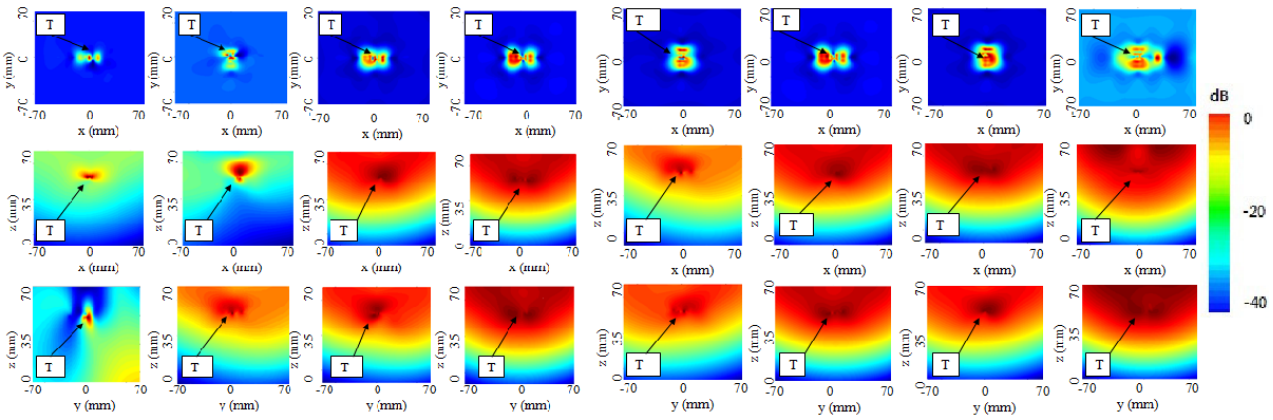

FIGURE 9. (a) Benign and (b) Malignant tumour positions (T) in x-y plane, x-z plane and y-z plane, in time domain, 5, 7 and 9 GHz, respectively.

using the intensities of the preprocessed transient signals and S_{11} parameters using (11).

A. IMAGING RESULTS

Fig. 9 (a) shows the 3-D cross-section images of the breast phantom. These images are obtained from the time domain signals, S_{11} at 5, 7 and 9 GHz respectively. The imaging results show that the benign tumour can be easily detected. Each of the images shows the correct position of the tumour. Specifically, the images obtained from the transient signals and S_{11} at 5 GHz shows a very clear tumour position with little surrounding noise. The 7 GHz images show the correct tumour position but the surrounding noise starts to interfere with the judgment of its position. The 9 GHz images show a butterfly-shaped energy distribution due to the power flow density becoming weak in the centre of the Vivaldi antenna when the working frequency increases. Fig. 9 (b) shows the 3-D images of the breast phantom with the embedded malignant tumour, using the time domain signals, S_{11} at 5, 7, 9 GHz. The resulting images show that the malignant tumour can be detected but with more noise compared with the benign one. Strong clutter is distributed around the malignant tumour images, especially at 9 GHz, due to its irregular and spiky morphology. The imaging results reveal the relationship between the cross-section images and the power flow density of the antenna. The time domain signals describe the tumour response across all whole working frequencies, while the frequency domain signals represent the detailed tumour response at different working frequencies. Furthermore, each working frequency corresponds to a different power flow density. At lower frequencies such as 5 GHz, the power density gathers in the centre front of the antenna, with more energy reflected, and this, results in clearer images. Conversely, the higher working frequency (9GHz, etc) results in relative blur images due to the dispersed power flow density. Not enough power is focused in the center of the antenna, given that the power flow density is a bidirectional radiation pattern, to illuminate the tumour. Therefore more noise is obtained from the multiple reflections such as from the edge of the antenna and the skin layer.

B. THE SINGULARITY EXPANSION OF MALIGNANT AND BENIGN TUMOUR RESPONSES

The imaging results show that both of the malignant and benign tumours can be detected with acceptable cross-section images. However, the image results cannot differentiate between malignant and benign tumours due to the accumulated noise and vague outline of the tumours. The principle of complex natural responses (CNRs), as introduced in Section IV, and malignant and benign tumours have for different morphologies giving different CNRs. The singularity expansion method (SEM) is a mathematical method used to extra the CNRs of the malignant and benign tumours. Fig. 9 shows the tumour positions, which can be utilized to estimate the boundary between ETR and LTR based on (10). Fig. 10 (a) illustrates that the estimated (dashed line) and the actual (solid line) boundaries are quite close, and this agreement, confirms the accuracy of the tumour position obtained from the imaging results as well as the LTR turn on time. A time window is used to eliminate the ETR and the clutters, with LTR remaining for further processing, as shown in Fig. 10 (b). Fig. 10 (c) and (d) show the calculated CNRs and the spectrum of the malignant and benign tumours, based on the actual and estimated LTR respectively. The results indicate that the estimated and actual CNRs are quite close. Besides, it can be observed that in general, the damping factors of the malignant tumour are greater than those of the benign tumour. On the other hand, the damping factors of both the malignant and benign tumours increase from 5 to 8 GHz, then falling down to the same level of the 7 GHz damping factor at around 9 GHz. Also, the spectrum of the benign tumour response is higher than that of the malignant tumour, ranging from 5 to 9 GHz. The observed results reveal the relationship between the morphology of the tumour and the damping factors as well as the spectrum of the received signals. Firstly, the morphological appearance of the tumour strongly affects the damping factors and the spectrum response. Specifically, a spiculated periphery causes stronger damping factors and a lower spectrum response than does a smoother periphery, due to the irregular surface scattering the incident wave in different directions. This phenomenon can be used to discriminate

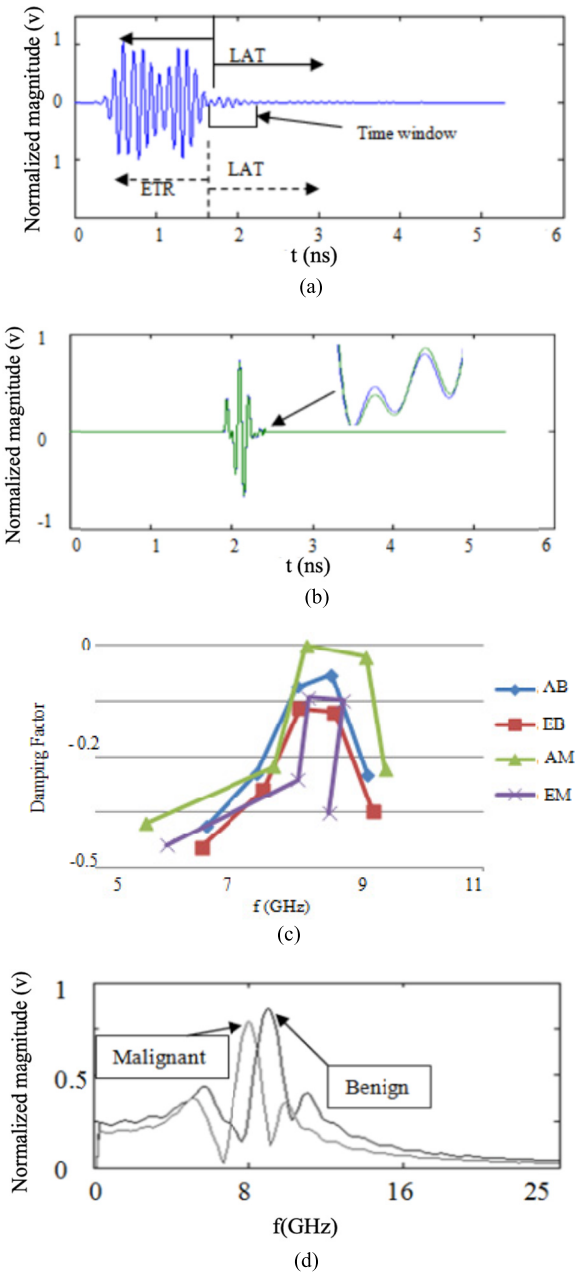

FIGURE 10. (a) The estimated LTR turn on time, (b) calibrated tumour response, (c) calculated damping factor and (d) spectrum of the benign and malignant tumour.

between malignant and benign tumours of the similar sizes, especially when the cross-section images of the cancerous breast cannot provide sufficient resolution.

V. CONCLUSION

This paper proposes a method based on complex natural responses (CNRs) as a complement to the current mono-static radar imaging system to characterize breast lesions in 3-D simulation. Two pathological phantoms, one with a benign and the other a malignant tumour embedded, are measured using the proposed mono-static imaging system to create the cross-section images in order to indicate the tumour positions. Both the malignant and benign tumours are correctly indicated in the resulting images. However, more noise accumulates around the malignant tumour, due to its spiculated periphery. Hence, the images of the malignant tumour have a more blurred boundary. Furthermore, images based on the time domain signals have lower noise levels than the frequency domain images since the former signals are average description of the whole working frequency range. Besides, the imaging results at 5 GHz provide clearer tumour location than those at 7 and 9 GHz since the bidirectional power flow density at higher frequencies causes the dispersive radiation from the Vivaldi antenna and the multiple reflections between the antenna edge and the skin layer, and therefore more noise gathered. Furthermore, the SEM based method is used to extract the complex natural resonances (CNRs) of the malignant and benign tumours. The results show that the damping factors increase when the surface of the tumour becomes more irregular, which means that the received signals from the malignant tumour have stronger damping factors. This is a potentially useful feature for distinguishing between malignant and benign tumours, especially when they are of similar size. Simulation results show that the use of the CNRs can successfully discriminate between a spherical benign tumour with a radius of 5 mm and a speculated periphery with an average radius of 5 mm. Further work will focus on the experimental work using a more realistic breast model to address various practical problems, and especially that of highly noisy environments. Besides, we are considering two approaches to achieve a better discrimination between the benign and malignant tumours. One way is to increase the working frequency of the antenna so that the image resolution can be improved. Another way is to employ the deep learning based semantic segmentation network such as U-net for tumour discrimination.

REFERENCES

[1] H. Song, X. Xiao, Z. Wang, and T. Kikkawa, "UWB microwave breast cancer detection with MRI-derived 3-D realistic numerical breast model," in *Proc. IEEE Int. Symp. Antennas Propag. USNC/URSI Nat. Radio Sci. Meeting*, Vancouver, BC, Canada, Jul. 2015, pp. 544–545, doi: 10.1109/APS.2015.7304658.

[2] M. M. Fakir, M. S. Ali, V. Vijayasarveswari, S. Khatun, and M. Jusoh, "Early breast health screening performance verification based on UWB imaging and neural network," in *Proc. 3rd Int. Conf. Electron. Des. (ICED)*, Thailand, Phuket, Aug. 2016, pp. 517–521, doi: 10.1109/ICED.2016.7804699.

[3] M. K. Sharma, M. Kumar, and J. P. Saini, "UWB-MIMO antenna with enhanced isolation for breast cancer detection," in *Proc. 2nd Int. Conf. Comput. Sustain. Global Develop. (INDIACom)*, New Delhi, India, 2015, pp. 787–790.

[4] Y. Masui, A. Toya, M. Sugawara, T. Maeda, M. Ono, Y. Murasaka, A. Iwata, and T. Kikkawa, "Differential equivalent time sampling receiver for breast cancer detection," in *Proc. IEEE Biomed. Circuits Syst. Conf. (BioCAS)*, Turin, Italy, Oct. 2017, pp. 1–4, doi: 10.1109/BIOCAS.2017.8325058.

[5] A. Afyf, L. Bellarbi, A. Achour, N. Yaakoubi, A. Errachid, and M. A. Sennouni, "UWB thin film flexible antenna for microwave thermography for breast cancer detection," in *Proc. Int. Conf. Electr. Inf. Technol. (ICEIT)*, Tangiers, MR, USA, 2016, pp. 425–429, doi: 10.1109/EITech.2016.7519635.

[6] R. Benjamin, "Synthetic, post-reception focusing in near-field radar," in *Proc. EUREL Int. Conf. Detection Abandoned Land Mines*, Oct. 1996, pp. 133–137.
[7] D. Gibbins, M. Klemm, I. J. Craddock, J. A. Leendertz, A. Preece, and R. Benjamin, "A comparison of a wide-slot and a stacked patch antenna for the purpose of breast cancer detection," *IEEE Trans. Antennas Propag.*, vol. 58, no. 3, pp. 665–674, Mar. 2010.
[8] R. Nilavalan, J. Leendertz, I. J. Craddock, R. Benjamin, and A. Preece, "Breast tumor detection using a flat 16 element array," in *Proc. 16th Int. Symp. Electromagn. Compat. Topical Meeting Biomed.*, 2005, pp. 81–84.
[9] Y. Xie, B. Guo, L. Xu, J. Li, and P. Stoica, "Multi-static adaptive microwave imaging for early breast cancer detection," in *Proc. 39th Asilomar Conf. Signals, Syst. Comput.*, 2005, pp. 285–289.
[10] R. Benjamin, I. J. Craddock, G. S. Hilton, S. Litobarski, E. McCutcheon, R. Nilavalan, and G. N. Crisp, "Microwave detection of buried mines using non-contact, synthetic near-field focusing," *IEE Proc. Radar, Sonar Navigat.*, vol. 148, no. 4, pp. 233–240, Aug. 2001.
[11] J. M. Sill and E. C. Fear, "Tissue sensing adaptive radar for breast cancer detection—Experimental investigation of simple tumor models," *IEEE Trans. Microw. Theory Techn.*, vol. 53, no. 11, pp. 3312–3319, Nov. 2005.
[12] R. M. Rangayyan, N. M. El-Faramawy, J. E. L. Desautels, and O. A. Alim, "Measures of acutance and shape for classification of breast tumors," *IEEE Trans. Med. Imag.*, vol. 16, no. 6, pp. 799–810, 1997.
[13] L. Peters, J. J. Daniels, and J. D. Young, "Ground penetration radar as a subsurface environmental sensing tool," *Proc. IEEE*, vol. 82, no. 4, pp. 1802–1821, Dec. 1994.
[14] C.-C. Chen and L. Peters, "Buried unexploded ordnance identification via complex natural resonances," *IEEE Trans. Antennas Propag.*, vol. 45, no. 11, pp. 1645–1654, Nov. 1997.
[15] Y. Chen, E. Gunawan, K. S. Low, S.-C. Wang, C. B. Soh, and T. C. Putti, "Effect of lesion morphology on microwave signature in 2-D ultra-wideband breast imaging," *IEEE Trans. Biomed. Eng.*, vol. 55, no. 8, pp. 2011–2021, Aug. 2008.
[16] Y. Huo, R. Bansal, and Q. Zhu, "Modeling of noninvasive microwave characterization of breast tumors," *IEEE Trans. Biomed. Eng.*, vol. 51, no. 7, pp. 1089–1094, Jul. 2004.
[17] E. Pancera, "Medical applications of the ultra wideband technology," in *Proc. Loughborough Antennas Propag. Conf. (LAPC)*, Nov. 2010, pp. 52–56.
[18] M. Klemm, I. Craddock, J. Leendertz, A. Preece, and R. Benjamin, "Experimental and clinical results of breast cancer detection using UWB microwave radar," in *Proc. IEEE Antennas Propag. Soc. Int. Symp.*, Jul. 2008, pp. 1–4.
[19] C. E. Baum, "On the singularity expansion method for the solution electromagnetic interaction problems," Air Force Weapons Lab, Kirtland AFB, Albuquerque, NM, USA, Tech. Rep. 88, 1971.
[20] C. E. Baum, "Singularity expansion of electromagnetic fields and potentials radiated from antennas or scattered from objects in free space," Air Force Weapons Lab, Kirtland AFB, Albuquerque, NM, USA, Tech. Rep. 179, 1973.
[21] M. Morgan, "Singularity expansion representations of fields and currents in transient scattering," *IEEE Trans. Antennas Propag.*, vol. 32, no. 5, pp. 466–473, May 1984.
[22] C. A. Balanis, *Advanced Engineering Electromagnetics*. Hoboken, NJ, USA: Wiley, 1989.
[23] E. Heyman and L. Felsen, "Creeping waves and resonances in transient scattering by smooth convex objects," *IEEE Trans. Antennas Propag.*, vol. AP-31, no. 3, pp. 426–437, May 1983.
[24] M. Van Blaricum and R. Mittra, "A technique for extracting the poles and residues of a system directly from its transient response," *IEEE Trans. Antennas Propag.*, vol. AP-23, no. 6, pp. 777–781, Nov. 1975.
[25] A. Poggio, M. Van Blaricum, E. Miller, and R. Mittra, "Evaluation of a processing technique for transient data," *IEEE Trans. Electromagn. Compat.*, vols. EMC–20, no. 1, pp. 165–173, Feb. 1978.
[26] H. Ouibrahim, D. D. Weiner, and T. K. Sarkar, "Matrix pencil approach to direction finding," *IEEE Trans. Acoust., Speech Signal Process.*, vol. ASSP-36, no. 4, pp. 610–612 Apr. 1988.
[27] S. K. Hong, W. S. Wall, T. D. Andreadis, and W. A. Davis, "Practical implications of poleseries convergence and the early-time in transient backscatter," NRL Memorandum, Washington, DC, USA, Tech. Rep. NRL/MR/5740–12-9411, Apr. 2012.

HAOYU ZHANG received the Ph.D. degree in electronic engineering from Edinburgh University, in 2015. He is currently a Senior Lecturer with Zhejiang Ocean University. His research interests include microwave imaging-based cancer detection and airborne SAR-based remote sensing.